Supporting Information

Fast Li^+ Conduction Mechanism and Interfacial Chemistry of a NASICON/Polymer Composite Electrolyte

Nan Wu[a,b,†], Po–Hsiu Chien[c,d,†], Yutao Li[a,*], Andrei Dolocan[a], Henghui Xu[a], Biyi Xu[a], Nicholas S. Grundish[a], Haibo Jin[b], Yan–Yan Hu[c,d], John B. Goodenough[a,*]

[a]Materials Science and Engineering Program and Texas Materials Institute, The University of Texas at Austin, Texas 78712, United States

[b]Beijing Key Laboratory of Construction Tailorable Advanced Functional Materials and Green Applications, School of Materials Science & Engineering, Beijing Institute of Technology, Beijing 100081, P. R. China

[c]Department of Chemistry and Biochemistry, Florida State University, Tallahassee, Florida 32306, United States

[d]Center of Interdisciplinary Magnetic Resonance, National High Magnetic Field Laboratory, 1800 East Paul Dirac Drive, Tallahassee, Florida 32310, United States

EXPERIMENT

Preparation of NASICON $LiZr_2(PO_4)_3$.

Stoichiometric amounts of Li_2CO_3, $(NH_4)_2HPO_4$, and $Zr(AC)_4$ were ground in a mortar and pestle, and sintered at 900 °C for 6 h. A 10 wt% Li_2CO_3 excess was used to compensate for the evaporation of Li_2O at high temperatures. The obtained powders were reground and fired at 1150 °C for 15 h in a Pt crucible. Finally, pellets of LZP powder were pressed and fired at 1150 °C for 10 h in a box furnace. Au was sputtered on the surfaces of the LZP pellet for Li^+ conductivity measurements. Raman spectroscopy was performed with a WITec Alpha 300 Raman microscope instrument equipped with a 532 nm wavelength laser for excitation.

Preparation of the composite polymer electrolytes.

PEO (Mw ~ 600,000) and Lithium bis(trifluoromethanesulfonyl)imide (LiTFSI) with a EO:Li molar ratio n =13:1 or 10:1 were first dissolved in anhydrous acetonitrile and stirred at 60 °C for 12 h to form a homogeneous solution. Different amounts of LZP powder was added to the solution as noted by the final composition of the composite; the mixture was cast onto a PTFE dish after stirring at 60 °C for 24 h. Finally, the PEO_n–LiTFSI–LZP CPE membrane was obtained by drying at 40 °C for 24 h in a vacuum. The membrane was stored in an Ar-filled glove box (H_2O < 1 ppm and O_2 < 1 ppm) until cells were prepared. Samples of PEO_n–LiTFSI and PEO_n–LiTFSI–15 wt% Al_2O_3 (PEO_n–LiTFSI–15Al_2O_3) were prepared under the same conditions. The thickness of the composite polymer electrolytes was controlled to be 200 μm.

Characterization of the composite polymer electrolytes.

The crystalline structure of the LZP pellet and the PEO–based composite membranes were investigated by X-ray diffraction (XRD) analysis with a Rigaku MiniFlex 600. The morphology of the composite membrane was characterized a FEI Quanta 650 scanning electron microscope (SEM). For the PEO_n–LiTFSI–LZP membrane, the Li^+ conductivity was tested in a symmetric SS|PEO_n–LiTFSI–LZP|SS (SS = stainless steel) cell from 30 to 80 °C. Electrochemical impedance spectroscopy (EIS) measurements were conducted on an Auto Lab PGSTAT 204 workstation with an AC amplitude of 10 mV and a frequency range from 1 MHz to 0.1 Hz. Linear sweep voltammetry was conducted with Li/composite membrane/SS coin cells at 40 °C.

The Li^+ transference number (t_{Li^+}) of the $P(EO)_{10}$–LiTFSI–LZP CPE membrane was calculated by a combination measurement of ac impedance and potentiostatic dc polarization according to modified Bruce–Vincent method.[1,2] In the experiment, a symmetric cell consisting of Li/polymer electrolyte/Li was applied a dc voltage (ΔV, and 10 mV in this study) until a steady current was obtained. Simultaneously, the ac impedance spectra of the same cell before and after the dc polarization were measured in the frequency range from 1 MHz to 0.1 Hz. The Li^+ transference number (t_{Li^+}) was then calculated using Eq. (1):[3,4]

$$t_{Li^+} = \frac{I_S R_{BS}[\Delta V - I_I R_{II}]}{I_I R_{BI}[\Delta V - I_S R_{IS}]} \quad (1)$$

Where I_I and I_S are the initial current and steady state current, R_{BI} and R_{BS} represent the bulk resistances before and after applying the dc voltage, R_{II} and R_{IS} are the respective interfacial resistances before and after the dc polarization.

Nuclear Magnetic Resonance Spectroscopy.

Solid–state magic–angle–spinning (MAS) ^{6}Li NMR measurements are recorded on a Bruker Avance III spectrometer at 11.75 T with the operating frequency of 73.6 MHz (^{6}Li). ^{6}Li NMR spectra are acquired using a 2.5–mm HXY Bruker probe spinning at a 25 kHz with one–pulse. A 90° pulse length of 4.75 μs and a recycle delay of 500 s is employed. ^{7}Li T_1 relaxation time is measured with inversion–recovery sequence. ^{6,7}Li chemical shift is referenced to solid LiCl at −1.1 ppm. A ^{6}Li/composite polymer/^{6}Li symmetric cell was cycled at 0.03 mA cm^{-2} for 100 h in the ^{6}Li→^{7}Li trace–exchange NMR measurement to study the Li^+ transport path in the composite polymer.

Flourier Transform Infrared Spectrometer.

Flourier transform infrared (FTIR) spectra of the composite polymer electrolytes were recorded using an Infinity Gold FTIR instrument covering the range of 400 to 4800 cm^{-1}. The composite polymer electrolytes were sealed by an ATR cell equipped with a germanium crystal in an Ar–filled glove box

Time-of-Flight Secondary Ion Mass Spectrometry.

TOF-SIMS was performed to analyze the chemical composition of the Li/solid electrolyte interface. Our setup consists of an ION–TOF TOF.SIMS 5 tool equipped with a Bi^+ analysis ion gun and a Cs^+ sputtering ion gun. During data acquisition the analysis ion gun was set either in the high current mode (HC, 30 keV ion energy, 3.7 pA measured sample current, 20 ns pulse width, >2 μm lateral resolution) for depth profiling or burst alignment mode (BA, 30 keV ion energy, 0.3 pA measured sample current, 100 ns pulse width, >200 nm lateral resolution) for high resolution mapping during cross–sectional imaging. All detected ions had negative polarity and the base pressure in the analysis chamber was kept at 10^{-9} mbar. The species of interest were detected with a mass resolution (m δm^{-1}) greater than 3000 in HC mode and 100 in BA mode. During depth profiling the Cs^+ sputtering beam (500 eV ion energy, ~40 nA measured sample current) was raster scanned over a 300 × 300 μm^2 area while the Bi^+ analysis ion beam was scanning a 100 × 100 μm^2 area centered within the regressing Cs^+ sputtered area. The depth profiles were acquired in noninterlaced mode, that is sequential sputtering and analysis (static SIMS). The sputtering rate of CPE(10:1)–25LZP was calculated by measuring the crater depth produced by the Cs^+ sputtering beam (Fig. S11) with a Keyence VK-X1100 confocal optical profilometer (404 nm laser scanning, 50x objective). A crater 33.035 μm deep was sputtered in 14 hours, leading to a sputtering rate of 0.655 nm s^{-1}. Before high lateral resolution mapping (BA mode imaging), the Li/solid electrolyte cross section was sputtered with

the Cs^+ ion beam for 6 hours over a 500 × 500 μm^2 area to remove any surface contamination and reduce the surface roughness. The BA mapping was then acquired over a 200 × 200 μm^2 area centered within the Cs^+ sputter–cleaned area. For depth profiling, the cycled and touched samples were stripped from the Li electrodes and the exposed solid electrolyte surface was analyzed. For cross–sectional imaging only one Li electrode was removed from the Li/solid electrolyte/Li stack and the remaining bilayer was mechanically sectioned with a sharp blade. After preparation, the samples were transferred from the argon-filled glove box to the TOF-SIMS analysis chamber in an in–house–designed, air–free transfer capsule.

Symmetric Li/Li cell.

A composite membrane was sandwiched between two identical lithium discs; the Li/composite membrane/Li was sealed in a 2032 coin cell for testing. The plating/stripping curves were collected with a Land CT2001A battery–testing system. The lithium metal was cleaned prior to cell assembly.

All–solid–state Li–metal batteries with $LiFePO_4$ and $LiNi_{0.8}Mn_{0.1}Co_{0.1}O_2$ cathode.

$LiFePO_4$, PEO, LiTFSI, and carbon black (60:20:10:10 in weight ratio) were mixed in anhydrous acetonitrile to form a homogeneous slurry, and the slurry was cast onto a carbon coated aluminum foil. The $LiFePO_4$ cathode film with an active material loading of (3–5) mg cm^{-2} was dried at 60 °C for 24 h in a vacuum. The NMC cathode film was prepared by coating the dimethylformamide (DMF) slurry with NMC (60 wt%), polyvinylidene fluoride (PVDF, 20 wt%), LiTFSI (10 wt%), and carbon black (10 wt%) onto a carbon coated aluminum foil. The composite NMC cathode was dried at 80 °C for 24 h in a vacuum. The mass loading of active material is (3–5) mg cm^{-2}. All–solid–state Li–metal batteries were assembled with a Li anode, a PEO_{10}–LiTFSI–25LZP membrane, and a $LiFePO_4$ or $LiNi_{0.8}Mn_{0.1}Co_{0.1}O_2$ (NMC) cathode in an Ar–filled glove box. As with the lithium symettric cells, the lithium metal was cleaned prior to cell assembly.

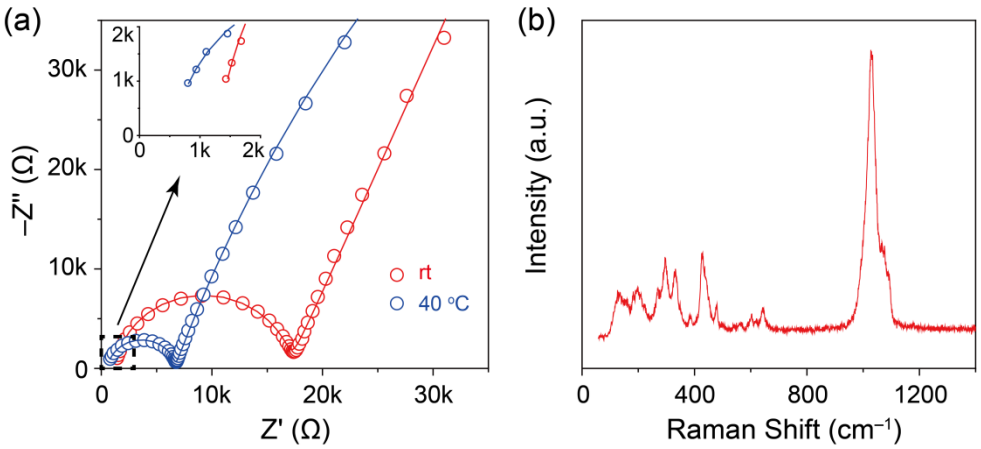

Supplementary Figure 1. Electrochemical impedance spectra (a) and Raman spectrum (b) of LZP pellet.

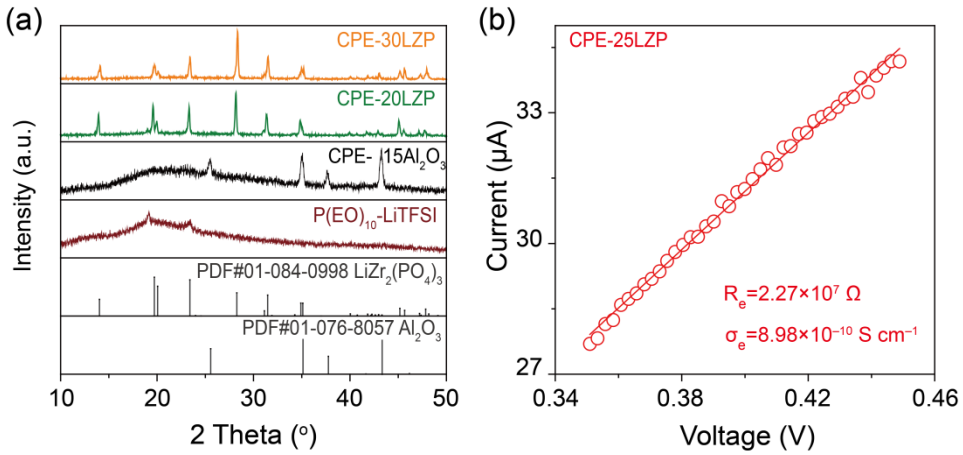

Supplementary Figure 2. XRD results (a) and electronic conductivity (b) of the composite polymer membrane.

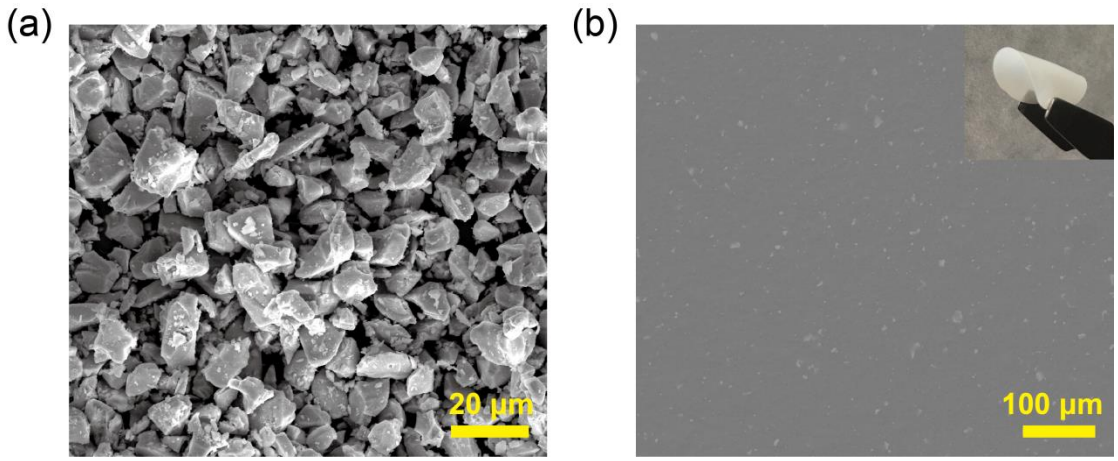

Supplementary Figure 3. SEM images of (a) LZP particles and (b) the CPE–25LZP membrane.

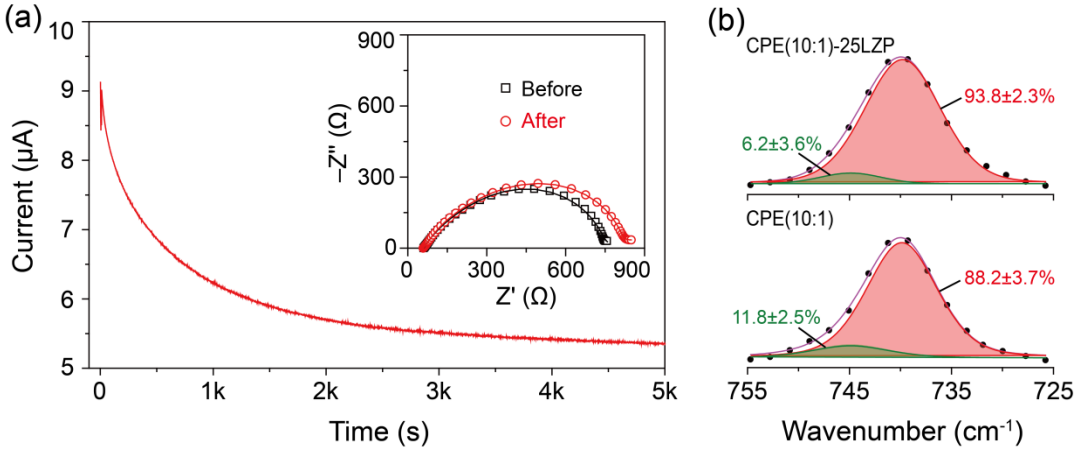

Supplementary Figure 4. (a) Time–dependent response of dc polarization (10 mV) in a symmetric Li/CPE–25LZP/Li cell; impedance plots of the cell before and after polarization (inset). (b) FTIR spectra of CPE-25LZP and CPE in the range of 755-725 cm^{-1}.

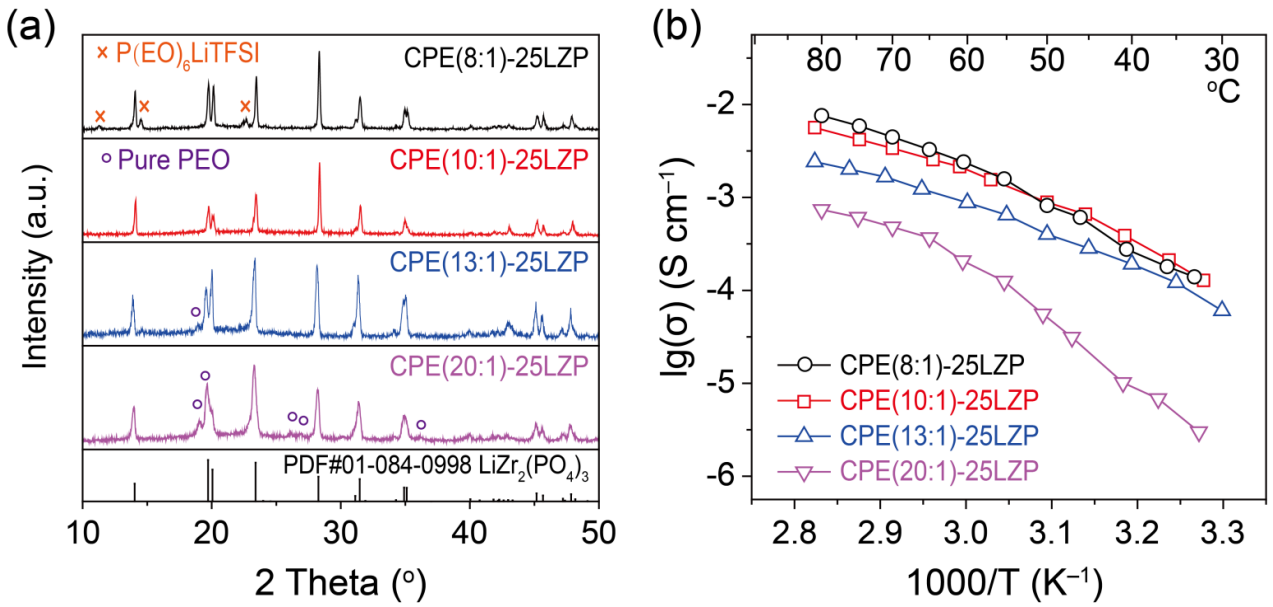

Supplementary Figure 5. (a) XRD patterns and (b) Arrhenius plots of CPE–25LZP with different [EO]/[Li^+] ratios (8:1, 10:1, 13:1, and 20:1).

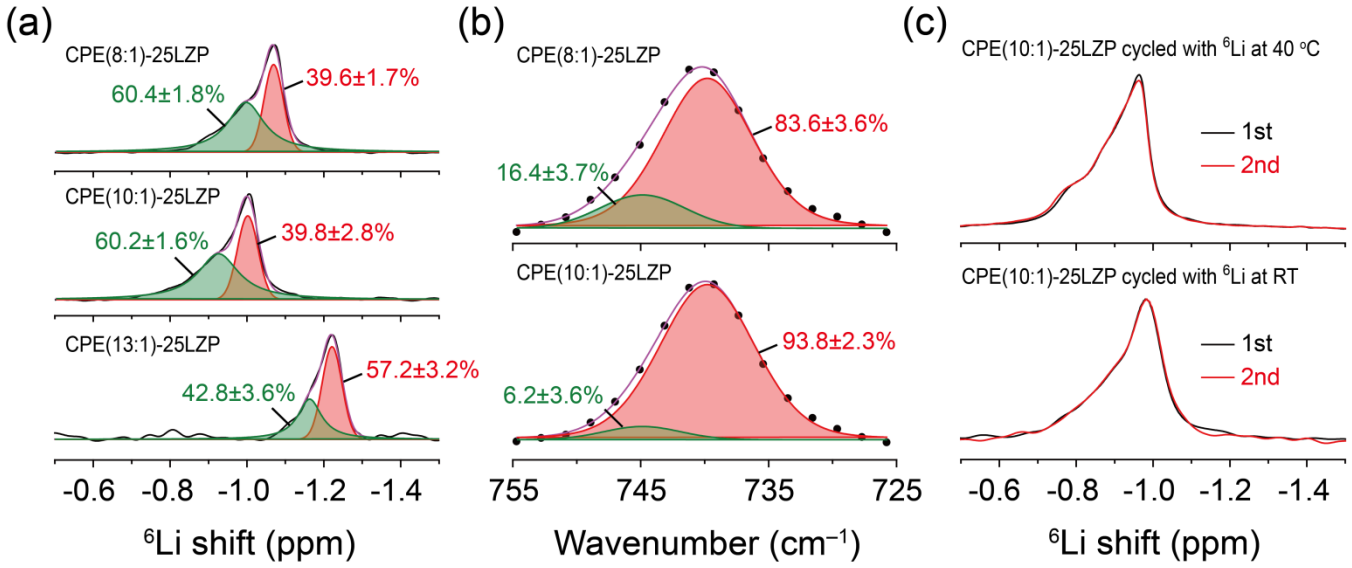

Supplementary Figure 6. (a) Solid–state ^{6}Li MAS NMR spectra of composite electrolytes with different [EO]/[Li^{+}] ratios, (b) FTIR spectra of CPE(8:1)–25LZP and CPE(10:1)–25LZP in the range of 755-725 cm^{-1}, and (c) comparison of the lineshapes of ^{6}Li cycled CPE(10:1)–25LZP at rt and 40 °C each set obtained in consecutive experiments.

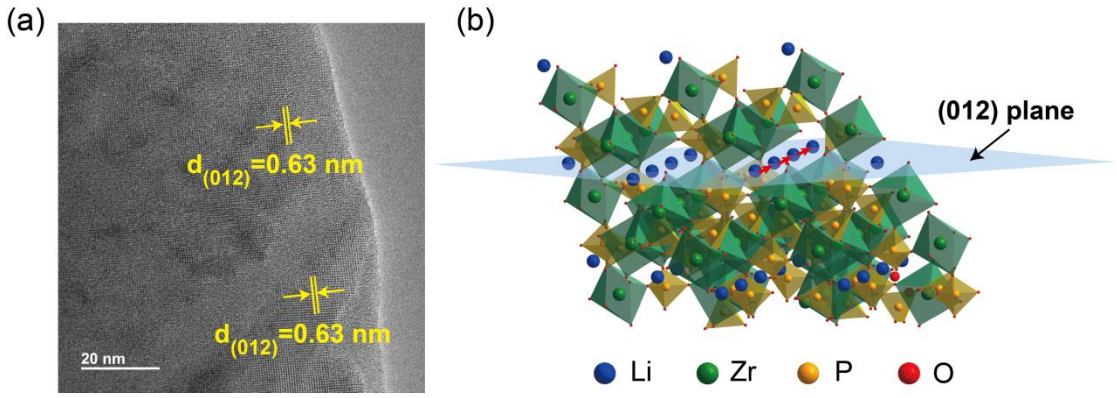

Supplementary Figure 7. (a) TEM image of LZP particle, (b) Li^+ transport on the exposed (012) crystal plane of LZP.

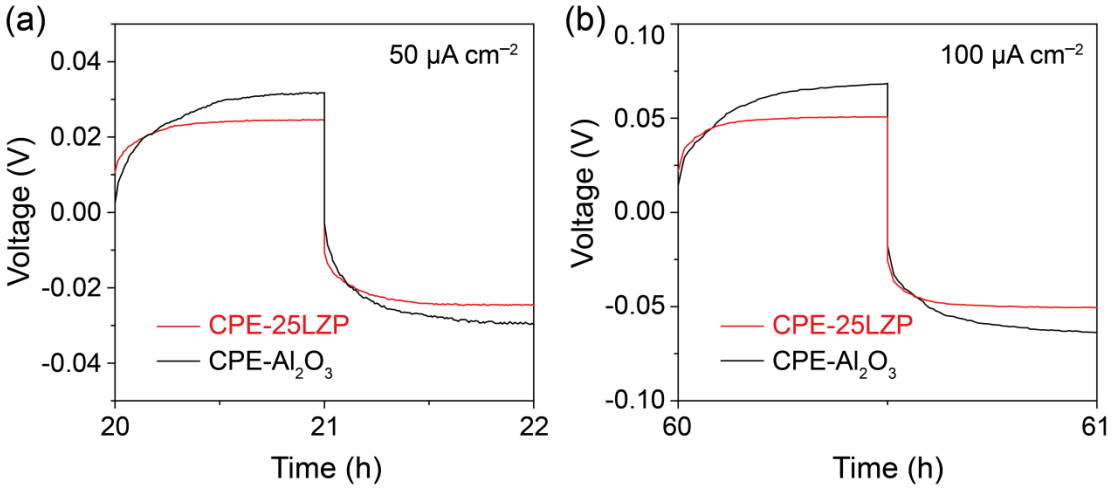

Supplementary Figure 8. Charge and discharge voltage profiles Li/Li cells at 40 °C at (a) 50 and (b) 100 μA cm^{-2}.

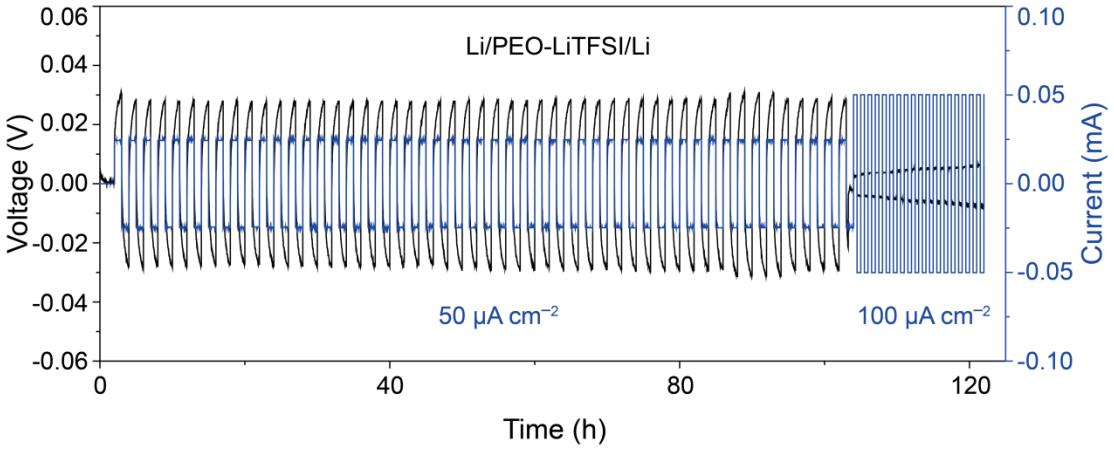

Supplementary Figure 9. The cycling of symmetric Li/PEO–LiTFSI/Li cell at 50 and 100 μA cm^{-2} at 40 °C. The cell short–circuited when cycled at 100 μA cm^{-2}.

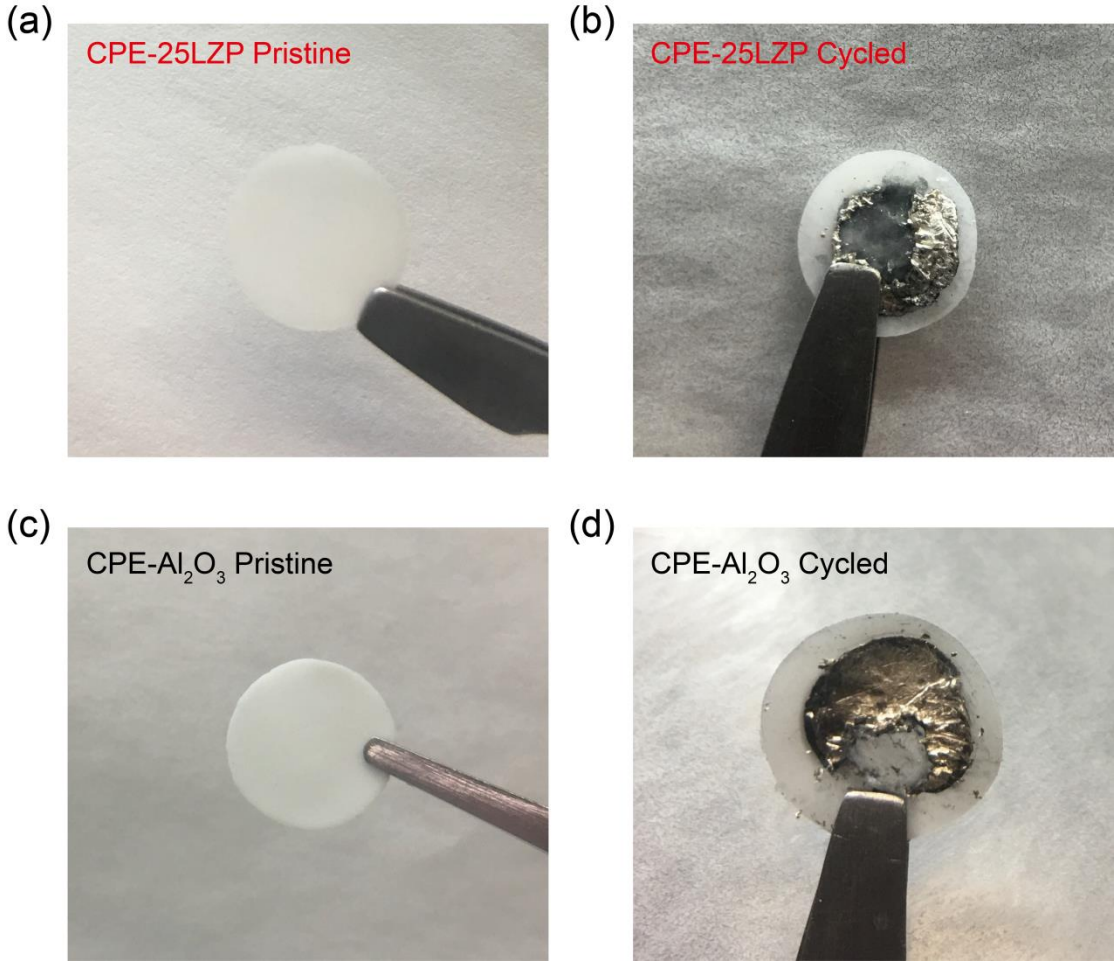

Supplementary Figure 10. Composite membrane before and after cycling in a symmetric Li/Li cell with (a–b) CPE–25LZP, and (c–d) CPE–15Al_2O_3.

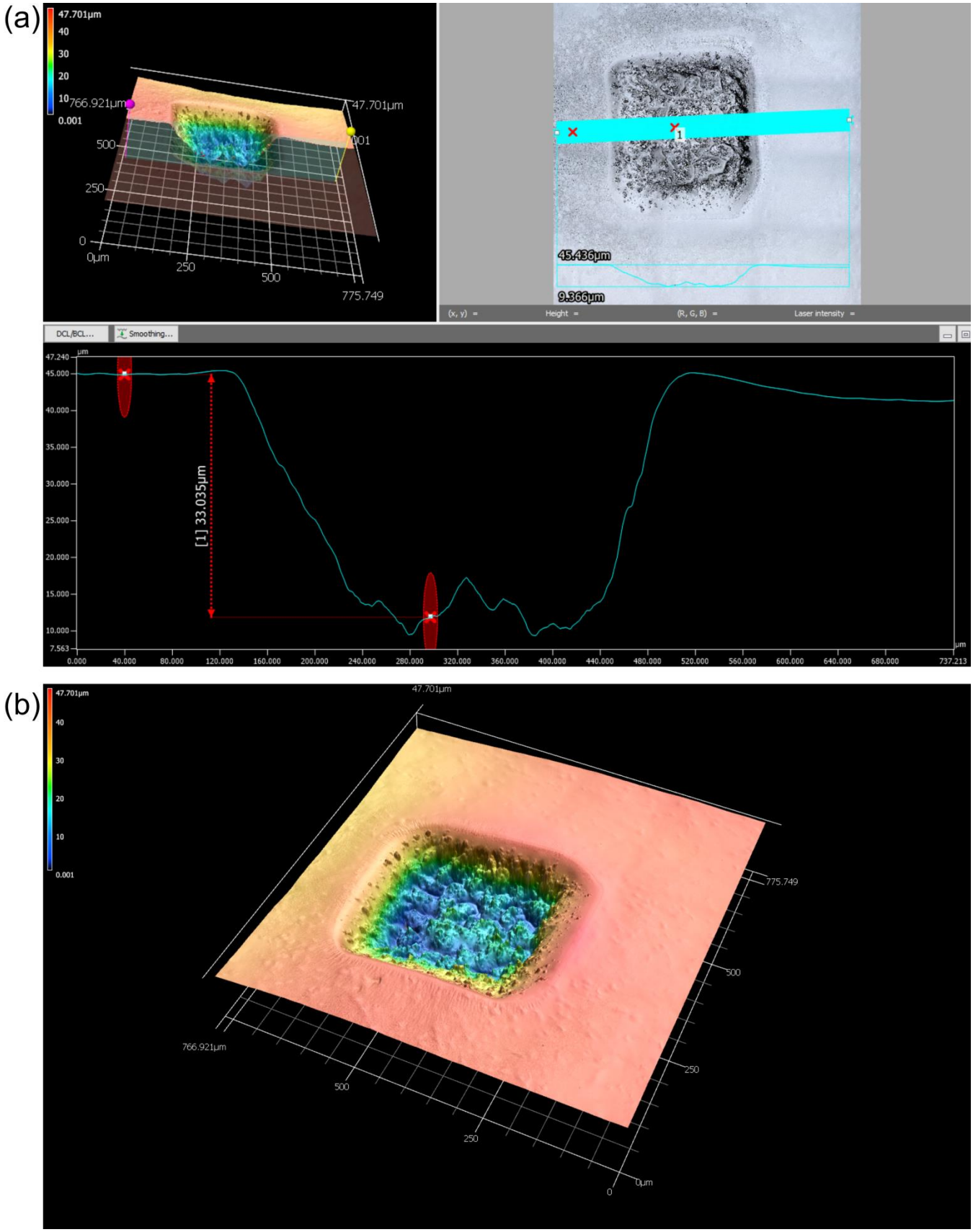

Supplementary Figure 11. (a) Depth profiling of the CPE(10:1)–25LZP, and (b) overview of the CPE(10:1)–25LZP after 14 hours of sputtering.

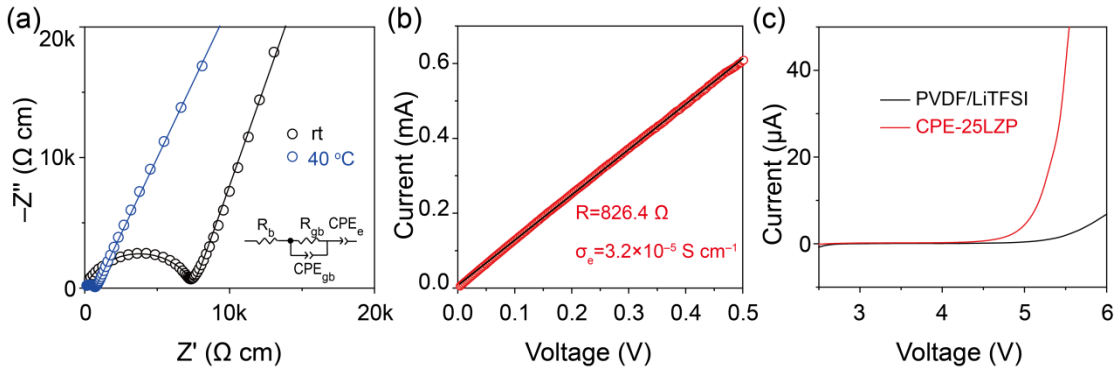

Supplementary Figure 12. (a) Electrochemical impedance spectra of PVDF–LiTFSI membrane, (b) electronic conductivity of the NMC cathode pellet composed of NMC, PVDF–LiTFSI and carbon (the thickness and area of the cathode is 80 μm and 0.3 cm^2, respectively), and (c) linear sweep voltammetry curve of PVDF–LiTFSI membrane.

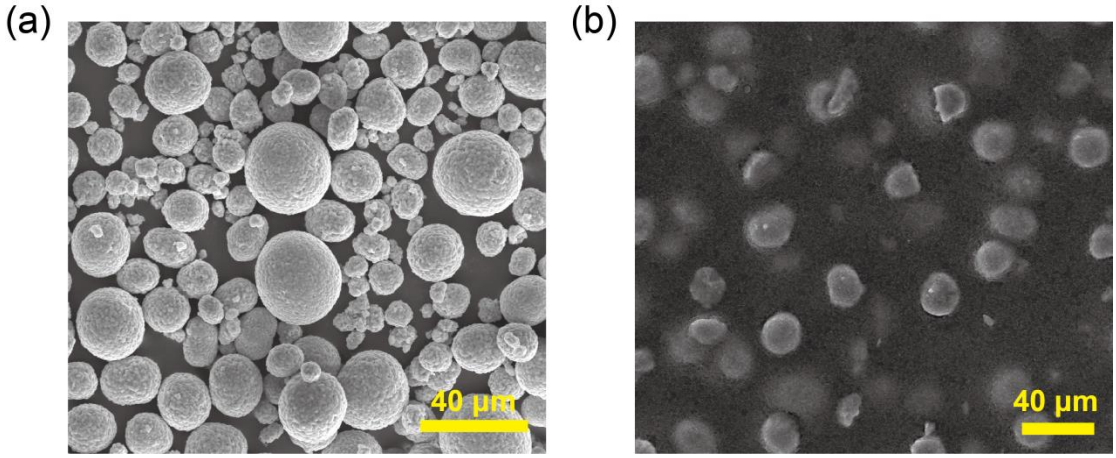

Supplementary Figure 13. (a–b) SEM image of the NMC cathode particles. (a) Pristine NMC cathode particles and (b) NMC particles uniformly coated by PVDF binder.

Supplementary Table 1. VTF fitting parameters for composite electrolytes with different [EO]/[Li^+] ratios.

Sample	E_a (eV)	A ($S \bullet K^{1/2} \bullet cm^{-1}$)	T_0 (K)	R^2
CPE(8:1)–25LZP	0.086	5.75	221.91	0.995
CPE(10:1)–25LZP	0.038	2.02	250.83	0.999
CPE(13:1)–25LZP	0.056	2.62	231.65	0.998
CPE(20:1)–25LZP	0.065	3.11	248.65	0.990

E_a: Pseudo–activation energy; A: Pre–exponential constant; T_0: Reference temperature which is close to the glass transition temperature; R^2: Correlation coefficient.

There are two prominent models to explain the temperature dependence of Li+ conductivity in solid electrolytes.

(1) Arrhenius Model: $\sigma(T) = \sigma_0 \exp\left[\frac{-E_a}{k_B T}\right]$, σ_0, E_a, and k_B are the pre–exponential factor, activation energy, and Boltzmann constant, respectively.

(2) Vogel–Tammann–Fulcher (VTF) Model: $\sigma = AT^{-1/2} \exp\left[\frac{-E_a}{k_B(T-T_0)}\right]$, where σ is the ionic conductivity, A is a pre–exponential constant, T is the absolute temperature, k_B is Boltzmann's constant, E_a is the pseudo–activation energy, and T_0 is the reference temperature which is close to the glass transition temperature.

The Arrhenius model is usually used for crystalline ionic conductors, (e.g. garnet $Li_7La_3Zr_2O_{12}$), where Li^+ conductivity is from a Li^+ jump to the nearest Li^+ vacancy rather than molecular motion. The VTF model explains ionic conductivity relations in amorphous polymer electrolytes and indicates that the Li^+ conductivity is from segmental motion of the polymer.[5]

Supplementary Table 2. Summary of ^{7}Li spin-lattice relaxation time (T_1) of composite electrolytes with different [EO]/[Li^+] ratios and different inorganic fillers.

	Composite electrolytes				
	CPE (13:1)	CPE (13:1)–15Al_2O_3	CPE (13:1)–25LZP		
	593 ± 9	544 ± 20	488 ± 34		
T_1 / ms	CPE (10:1)	CPE (10:1)–15Al_2O_3	CPE (10:1)–25LZP	CPE (10:1)–25LZP cycled with ^{6}Li at RT	CPE (10:1)–25LZP cycled with ^{6}Li at 40 °C
	468 ± 7	418 ± 8	382 ± 13	401 ± 8	434 ± 18
	CPE (8:1)	CPE (8:1)–15Al_2O_3	CPE (8:1)–25LZP		
	427 ± 10	N/A	379 ± 33		

The increase in activation energy follows an increase in the Arrhenius pre–factor, *A*; hence, the results derived from VTF analysis agree with the Meyer–Neldel rule.[6] However, excluding CPE(20:1)-25LZP, a discrepancy between ^{7}Li relaxation rates ($1/T_1$) and the pre–factor is noticed. Before seeking a reasonable explanation for the relationship between the pre–factor (A) and the Li^+ ion mobility probed with ^{7}Li T_1 relaxation, we needed to consider the following factors dictating the magnitude of the pre–factor. Th e pre–factor is influenced by the attempt frequency (ν_0), the concentration of mobile Li^+, and the migration entropy (ΔS). Higher activation energy is often related to a higher attempt frequency.[7] Also, higher migration entropy can be expected when more paths to the activated sites are involved as more thermal energy is provided.[7] We reason that the concentration of mobile Li^+ that effectively participates in ion conduction determines the overall Li^+ mobility if the interaction between the unsaturated Li^+ (Li^+_{unsat}) in LZP and O_{PEO} remains nearly unchanged in all CPE–25LZP. From CPE(10:1)–25LZP to CPE(13:1)–25LZP, the activation energy increases, whereas the ^{7}Li relaxation rate drops from 2.62 s^{-1} to 2.05 s^{-1}. When more LiTFSI was added in an attempt to increase the Li–ion conductivity, similar ^{7}Li relaxation rates were detected in CPE(10:1)–25LZP (2.62 s^{-1}) and CPE(8:1)–25LZP (2.64 s^{-1}), indicating comparable Li^+ mobility. The attempt frequency (Table S1) should have increased significantly in CPE(8:1)–25LZP (A = 5.75 S•$K^{1/2}$•cm^{-1}), but the undissolved LiTFSI (or clustered LiTFSI) revealed by FTIR (Figure S6b) hints that the effective Li^+ was not sufficiently enhanced to enable faster Li^+ mobility. These results suggest that multiple factors affect the Li–ion conductivity in CPE and the fraction of the effective mobile Li^+ needs to be carefully considered when optimizing the Li-ion conductivity in these systems.

Supplementary Table 3. Interfacial resistance between solid electrolytes and Li metal/$LiFePO_4$ cathode

Sample	Li/electrolyte (Ω cm^{-2})	Cathode/electrolyte (Ω cm^{-2})	Measure Temperature (°C)	Reference
$P(EO)_{20}$–LiTFSI	50	N/A	80	3
$P(EO)_{18}$–LiTFSI–1% LGPS	26	N/A	80	8
$P(EO)_{18}$–LiTFSI–modified SiO_2	71.8	N/A	60	9
$P(EO)_{15}$–$LiClO_4$–0.5LLZTO	325	N/A	60	10
$P(EO)_{15}$–LiTFSI–LLZO	70	N/A	60	11
$P(EO)_{10}$–LiTFSI	N/A	74.5~308	50	12
$P(EO)_{15}$–LiTFSI–Al_2O_3	N/A	275	45	13
$P(EO)_{10}$–LiTFSI–25LZP	175	100	40	This work

REFERENCES

(1) Evans, J.; Vincent, C. A.; Bruce, P. G. Electrochemical measurement of transference numbers in polymer electrolytes. *Polymer* **1987**, *28*, 2324.

(2) Abraham, K. M.; Jiang, Z.; Carroll, B. Highly Conductive PEO-like Polymer Electrolytes. *Chem. Mater.* **1997**, *9*, 1978.

(3) Zhang, H.; Liu, C.; Zheng, L.; Xu, F.; Feng, W.; Li, H.; Huang, X.; Armand, M.; Nie, J.; Zhou, Z. Lithium bis(fluorosulfonyl)imide/poly(ethylene oxide) polymer electrolyte. *Electrochim. Acta* **2014**, *133*, 529.

(4) Han, H.-B.; Liu, K.; Feng, S.-W.; Zhou, S.-S.; Feng, W.-F.; Nie, J.; Li, H.; Huang, X.-J.; Matsumoto, H.; Armand, M.; Zhou, Z.-B. Ionic liquid electrolytes based on multi-methoxyethyl substituted ammoniums and perfluorinated sulfonimides: Preparation, characterization, and properties. *Electrochim. Acta* **2010**, *55*, 7134.

(5) Aziz, S. B.; Woo, T. J.; Kadir, M. F. Z.; Ahmed, H. M. A conceptual review on polymer electrolytes and ion transport models. *J. Sci.: Adv. Mater. Devices* **2018**, 3, 1-17.

(6) Meyer, W.; Neldel, H. Concerning the relationship between the energy constant epsilon and the quantum constant alpha in the conduction-temperature formula in oxydising semi-conductors. *Phys. Z.* **1937**, 38, 1014–1019.

(7) Yelon, A.; Movaghar, B. Microscopic explanation of the compensation (Meyer-Neldel) rule. *Phys. Rev. Lett.* **1990,** *65*, 618-620.

(8) Zhao, Y.; Wu, C.; Peng, G.; Chen, X.; Yao, X.; Bai, Y.; Wu, F.; Chen, S.; Xu, X. A new solid polymer electrolyte incorporating $Li_{10}GeP_2S_{12}$ into a polyethylene oxide matrix for all-solid-state lithium batteries. *J. Power Sources* **2016**, 301, 47-53.

(9) Liu, S.; Imanishi, N.; Zhang, T.; Hirano, A.; Takeda, Y.; Yamamoto, O.; Yang, J. Effect of nano-silica filler in polymer electrolyte on Li dendrite formation in Li/poly(ethylene oxide)–$Li(CF_3SO_2)_2N$/Li. *J. Power Sources* **2010**, 195, 6847-6853.

(10) Cheng, S. H.-S.; He, K.-Q.; Liu, Y.; Zha, J.-W.; Kamruzzaman, M.; Ma, R. L.-W.; Dang, Z.-M.; Li, R. K. Y.; Chung, C. Y. Electrochemical performance of all-solid-state lithium batteries using inorganic lithium garnets particulate reinforced PEO/$LiClO_4$ electrolyte. *Electrochim. Acta* **2017**, 253, 430-438.

(11) Keller, M.; Appetecchi, G. B.; Kim, G.-T.; Sharova, V.; Schneider, M.; Schuhmacher, J.; Roters, A.; Passerini, S. Electrochemical performance of a solvent-free hybrid ceramic-polymer electrolyte based on $Li_7La_3Zr_2O_{12}$ in $P(EO)_{15}$LiTFSI. *J. Power Sources* **2017**, 353, 287-297.

(12) Hanai, K.; Kusagawa, K.; Ueno, M.; Kobayashi, T.; Imanishi, N.; Hirano, A.; Takeda, Y.; Yamamoto, O. Interfacial properties between $LiFePO_4$ and poly(ethylene oxide)–$Li(CF_3SO_2)_2N$ polymer electrolyte. *J. Power Sources* **2010**, 195, 2956-2960.

(13) Tan, R.; Gao, R.; Zhao, Y.; Zhang, M.; Xu, J.; Yang, J.; Pan, F. Novel Organic–Inorganic Hybrid Electrolyte to Enable $LiFePO_4$ Quasi-Solid-State Li-Ion Batteries Performed Highly around Room Temperature. *ACS Appl. Mater. Interfaces* **2016**, 8, 31273-31280.